GFZ
Helmholtz-Zentrum
POTSDAM

HELMHOLTZ-ZENTRUM POTSDAM
DEUTSCHES
GEOFORSCHUNGSZENTRUM

Shafe, A. A., Hossain, M. D., Benamara, M., Roddatis, V., Mayanovic, R. A. (2023): Defects and Surface Chemistry of Novel PH-Tunable NiO-Mn3O4 ± MnxNi1-xO Heterostructured Nanocrystals as Determined Using X-ray Photoemission Spectroscopy. - Journal of Electronic Materials, 53, 1193-1202.

https://doi.org/10.1007/s11664-022-10047-5

Institional Repository GFZpublic: https://gfzpublic.gfz-potsdam.de/

Defects and surface chemistry of novel pH-tunable NiO-Mn_3O_4±$Mn_xNi_{1-x}O$ heterostructured nanocrystals as determined using X-Ray photoemission spectroscopy

Abdullah Al Shafe [1], Mohammad Delower Hossain [2], Mourad Benamara[3] Vladimir Roddatis[4], and Robert A. Mayanovic[1]

[1] Department of Physics, Astronomy and Materials Science, Missouri State University, Springfield, MO 65897, USA
[2] Department of Materials Science and Engineering, The Pennsylvania State University, University Park, PA 16802, USA
[3]University of Arkansas, Fayetteville, AR 72701, USA
[4]GFZ German Research Centre for Geosciences, Telegrafenberg 14473, Potsdam, Germany

E-mail: RobertMayanovic@MissouriState.edu

Abstract

We have developed a novel set of (Mn_3O_4 and/or $Mn_xNi_{1-x}O$)/NiO heterostructured nanocrystals (HNCs) that show promise for multifunctionality. A two-step procedure was used to synthesize our HNC samples. Thermal decomposition was first used to synthesize NiO core nanoparticles whereas hydrothermal synthesis under varying pH conditions was subsequently used to produce overgrowth of a $Mn_xNi_{1-x}O$ shell and/or Mn_3O_4 islands on the NiO core. In this work, we report on the investigation of the defects and surface/interface chemistry of our HNC samples using x-ray photoelectron spectroscopy (XPS). The results from a detailed analysis of the Mn 2p XPS spectra show that the Mn^{3+}:Mn^{2+} ratio increases with increasing pH value used in synthesis of the samples. This is consistent with a trend toward predominance of Mn_3O_4 islands at higher pH values, a predominance of $Mn_xNi_{1-x}O$ shell in the lowest pH values and a mixture of both for intermediate pH values. A reduction of the satellite features of the Ni 2p XPS with increasing pH of the synthesis medium is attributed predominantly to surface/interface defects of the HNCs. Fitting of the O 1s XPS spectra shows that Ni-OH and Mn-OH are likely the dominant contribution to the lateral peak whereas defects such as oxygen in an oxygen deficient environment and/or oxygen vacancies comprise a smaller contribution. Analysis of both the Ni 2p and O 1s XPS measured from our samples shows evidence only for a Ni^{2+} chemical environment (i.e., negligible Ni^{3+}) in octahedral coordination consistent with a rocksalt structure and well-ordered NiO or $Mn_xNi_{1-x}O$ nanomaterial. The presence of point defects and the nature of the surface/interface chemistry as determined using XPS suggests that our HNC samples may also be suitable for heterogeneous catalysis applications.

Keywords: Magnetic nanocrystal, XPS analysis, Auger peak, Multiplet Splitting, TEM, XRD

Introduction

Owing to advances made in the field of nanoscience, heterostructured nanocrystals (HNCs) have attracted considerable attention due to their multifunctionality, versatility, and novel physicochemical properties [1–3]. The HNCs, which are typically comprised of two or more distinct structural phases bonded directly at heterointerfaces, have been developed to overcome the challenges posed by conventional single-material nanoparticles or nanostructures. Controlled synthesis of the HNCs has led to the architectural control of their shape and physicochemical properties for use in numerous applications. For example, the magnetic heterostructured nanocrystals exhibit unique nanoscale magnetic properties, including enhanced coercivity, increased saturation magnetization and magnetic exchange bias, which can be tailored for novel magneto-optical or spintronic devices [4–6]. Many magnetic HNCs exhibit multifunctionality as demonstrated in their adoption for electronic applications, such as for FET, memory, solar cell, photovoltaic, and laser devices [4], [7]. The transition-metal-oxide HNCs also provide significant potential for biomedical applications, including for drug delivery, as MRI agents, biosensors, and for multimodal imaging [8–11]. In particular, a number of magnetic HNCs exhibit fast resistance switching phenomena, which is ideal for nonvolatile memory device applications [12,13], as well as enhanced exchange bias effects [14], which can be used to exceed the superparamagnetic limit [14,15].

The coupling of an antiferromagnetic (AFM) and either a ferro- (FM) or ferrimagnetic (FiM) phase in bimagnetic HNCs has provided for substantial enhancement and change in the magnetic behavior of such nanostructures, particularly as manifested in the magnetic properties which are directly impacted by the exchange bias effect [16–19]. One of the determinative factors affecting the exchange bias in bimagnetic HNCs is the quality of the core/overgrowth interface [20,21]. Depending upon the degree of lattice mismatch between the core and overlayer structural phases, defects such as misfit dislocations, vacancies, stacking faults and lattice strain are often present at the core/overgrowth interfaces of HNCs. It is presently still not entirely clear how such defects impact upon the nature and degree of the exchange bias that can result in bimagnetic HNCs. We have been able to manipulate such effects in our previous work on AFM/FiM coupled $Cr_2O_3/M_xCr_{2-x}O_3$ core-shell nanoparticles [20–24] and (Mn_3O_4 and/or $Mn_xNi_{1-x}O$)/NiO bimagnetic HNCs [25]. Our previous study demonstrated that overgrowth of Mn_3O_4 and/or $Mn_xNi_{1-x}O$ phases and the resulting magnetic properties are tunable using pH in the hydrothermal synthesis of (Mn_3O_4 and/or $Mn_xNi_{1-x}O$)/NiO HNCs [26]. In particular, it was shown that a substantially large coercivity and exchange bias is obtainable for the Mn-NiO-based HNCs upon tuning the pH value to about 5 in the second step hydrothermal synthesis process [26]. During hydrothermal synthesis, Mn^{2+} and Mn^{3+} ions are adsorbed on the NiO surface, competing with the highly reactive OH^- ions present in the aqueous solutions. The adsorption of the metal ions on the NiO surface is controlled via the protonation and deprotonation processes, and thereby pH, as described in more detail in our previous work [26]. Accordingly, pH has a direct affect on the structural composition of the overgrowth phase and defect properties of the core/overgrowth interface [27–29].

Notably, our (Mn_3O_4 and/or $Mn_xNi_{1-x}O$)/NiO HNCs are a completely novel heterostructured metal oxide system having multivalent Mn oxidation states: Consequently, these nanostructures have potential for multifunctionality and may have particular promise for heterogeneous catalysis applications. Although studies on nanoscale $Mn_xNi_{1-x}O$ are sparse, it has been shown that $Mn_xNi_{1-x}O$ nanoparticles supported on Si are an efficient catalyst of methane [30,31]. Conversely, several studies have shown nanostructured Mn_3O_4 to be potentially useful for heterogenous catalysis. Studies have demonstrated that morphology and crystallographic orientation of active surfaces of Mn_3O_4 nanoparticles have a direct bearing on the efficacy of catalysis [32,33]. Yang et al. found that a combination of nanoparticulate Mn_3O_4, NiO, and Ni on carbon nanotube supports performed well in the catalysis of benzyl alcohol [34]. Imboon et al. (2021) showed that Mn_3O_4 nanoparticles supported on graphene oxide are an efficient photo-catalyst which they attributed to the formation of vacancy defects in the nanoparticles [35]. Because the catalytic reactions occur predominantly at surface and interface regions of HNCs, a detailed XPS study of our novel heterostructured nanoparticulate samples containing Mn_3O_4, NiO, and $Mn_xNi_{1-x}O$ is much needed. A detailed study of the morphological, structural and magnetic properties of our pH-tuned (Mn_3O_4 and/or $Mn_xNi_{1-x}O$)/NiO HNC samples has been published previously [26]. In the present work, we focus on a study of the same samples using X-ray photoelectron spectrometry (XPS), to gain better insight into the metal cation oxidation state characteristics, core/overgrowth surface chemical environment and surface/interface defects of the (Mn_3O_4 and/or $Mn_xNi_{1-x}O$)/NiO HNCs.

Experimental

The NiO nanoparticles used to obtain the HNCs were first synthesized via the thermal decomposition technique [36]. A $Ni(OH)_2$ powder was obtained upon reaction of $NiCl_2.6H_2O$, NaOH and $N_2H_4.H_2O$, taken at a ratio of 1:5:10, respectively. The chemicals were combined in an absolute ethanol solution and mixed for about 3 hours using a magnetic stirrer. The molar concentration of the $NiCl_2.6H_2O$ was maintained at 0.11M. After thorough mixing of the constituents, $Ni(OH)_2$ was formed as a precipitate via the following reactions:

$$NiCl_2.6H_2O + 6C_2H_5OH \rightarrow [Ni(C_2H_5OH)_6]Cl_2 \quad (1)$$

$$[Ni(C_2H_5OH)_6]Cl_2 + mN_2H_4 \rightarrow 6C_2H_5OH + [Ni(N_2H_4)m]Cl_2 \quad (2)$$

$$[Ni(N_2H_4)m]Cl_2 + 2KOH \rightarrow mN_2H_4 + Ni(OH)_2 \quad (3)$$

Subsequently, the $Ni(OH)_2$ precursor was placed in an oven at 600 ^oC for 2 hours where it transformed into NiO nanoparticles [$Ni(OH)_2 \rightarrow NiO + H_2O$] in air. In preparation for the second step in the synthesis process, approximately 80 ml of deionized water (DI) was de-oxygenated by passing dry N_2 gas through it at 65-70 ^oC for 15-

20 minutes. The flow rate of the N_2 gas was set at ~2 L/min typically resulting in a reduction from an initial dissolved oxygen level in water of ~9 mg/L to less than 0.5 mg/L. The NiO nanoparticles, at a quantity of 0.33gm, and 0.5M $MnCl_2 \cdot 3H_2O$ were added to the de-oxygenated DI water. The pH of the aqueous solution containing the NiO nanoparticles was adjusted using HCl or NaOH and subsequently sonicated for 25-30 minutes. The Mn-bearing aqueous solution containing NiO nanoparticles was sealed in a Teflon-lined autoclave and heated in an oven at 200 ^oC for 22.5 hours, for each sample. More details regarding our hydrothermal synthesis method can be found elsewhere [22]. The final HNC product was then washed thoroughly with DI water and dried in air. As described previously, eight different samples were prepared at solution pH values ranging from 2.4 to 7.0 [26]. The size, as obtained from analysis of the XRD data measured from the HNC samples, pH values used in their synthesis, the coercivity, and exchange bias of the samples are shown in Table I [26].

Table I: The pH value used in hydrothermal synthesis, particle size, coercivity and exchange bias for the samples of this study

Sample	Sol. pH	Size (nm)	Coercivity (Oe)*	Exchange Bias (Oe)*
B1	2.4	29.34	511.3	165.5
B2	3.0	29.69	934.3	620.8
B3	3.5	28.74	826.0	602.0
B4	4.0	29.24	1530.0	1670.9
B5	4.5	25.03	2350.7	2199.9
B6	5.0	27.74	5860.4	2952.5
B7	6.0	25.53	4122.9	1444.6
B8	7.0	24.89	1011.5	833.1

*From Shafe et. al. [26]

The XPS analysis of the HNC samples was made using a Versa Probe XPS (Physical Electronics) with monochromated K-α x-rays from an aluminum source at 1486 eV. A pass energy of 117.4 eV was used for survey scans and 58.7 eV or below was used for high-resolution scans. The source and analyzer of the XPS instrument were calibrated using the Ag $3d_{5/2}$ (FWHM = 0.36 eV) peak having characteristic energy of 368.26 eV. An Alpha 110 hemispherical analyzer (Thermo Scientific) having a pass energy of 25 eV was used to collect the XPS spectra. High-resolution XPS scan were collected in the 840 - 890 eV binding energy (B.E.) range for the Ni 2p region, the 520 - 540 eV B.E. range for the O 1s region and the 626 - 660 eV B.E. range for the Ni Auger/Mn 2p region. XPS data analysis and peak fitting were performed using CasaXPS 2.3.16 software and the calibration was made using a C 1s peak (284.8 eV) originating from the carbon tape used to hold the samples in the instrument. For quantitative analysis, the software uses corrected Relative Sensitivity Factor (RSF) values of 93.683 for Ni 2p, 16.732 for O 1s, and 67.281 for the Mn 2p region. TEM samples were prepared using hexane as a solvent and a probe sonicator for proper dispersion of the nanocrystals. The HNCs were dispersed on carbon lacey grids for TEM imaging. Images and data were collected using a ThermoFisher Scientific Themis Z Cs aberration corrected Scanning Transmission Electron Microscope (S/TEM) operated at 300 kV and located at the PISA facility GFZ, Potsdam, Germany. The images were analyzed using ImageJ software.

Results and discussions

As reported previously, our Rietveld refinement fitting of the XRD data and analysis of the STEM images and STEM-EELS mapping used to characterize the NiO nanoparticles and B1 – B8 HNC samples provided evidence for a pH-dependent topotaxial Mn_3O_4 and/or epitaxial $Mn_xNi_{1-x}O$ overgrowth on NiO core nanocrystals [26]. A rocksalt-structured $Mn_xNi_{1-x}O$ overgrowth on the same structured ($Fm\bar{3}m$) NiO core was found to be highly predominant only for sample (B1) prepared at the lowest pH value (2.4). A combination of the $Mn_xNi_{1-x}O$ and spinel-structured (I41/amd) Mn_3O_4 overgrowth phases were found to be present for the $2.4 < pH < 4.5$ range (B2 – B5)

whereas the Mn_3O_4 overgrowth was found to be the predominant phase for pH > 4.5 (B6 - B8) of solution used in the hydrothermal synthesis of the HNCs [26] (see Table I for sample designation). Furthermore, the results from the SQUID and PPMS magnetometry measurements made on the HNC samples were found to be consistent with the XRD and TEM results: The exchange bias and coercivity fields were highest (~3.0 and 5.9 KOe, respectively) for the sample (B6) prepared at a pH of 5 [26]. Due to lattice mismatch and core-overgrowth structural phase differences (i.e., NiO vs Mn_3O_4), lattice strain effects, structural reorientation and defect formation as described above are possible at the core/overgrowth interface of the B1 – B8 HNC samples. The results from our Rietveld refinement fitting of XRD spectra showed that the average lattice parameters (*a*) of NiO core and $Mn_xNi_{1-x}O$ overgrowth are 4.175 Å and 4.181 Å, respectively, whereas the Mn_3O_4 overgrowth has average lattice parameters of a = 5.81 Å and c = 9.80 Å, for the B1 – B8 HNC samples [26]. This gives a lattice mismatch between the NiO and $Mn_xNi_{1-x}O$ phases of 0.14%. We showed in our previous study that the spinel-structured (hausmannite) Mn_3O_4 overgrowth phase, having octahedral and tetrahedral sites occupied by Mn^{3+} and Mn^{2+} ions, respectively, reorients to accommodate the alignment of the core/overgrowth cations resulting in topotaxial growth along the <111> preferred direction [26]. Evidence for such reorientation of the Mn_3O_4 nano-island overgrowth on NiO core nanoparticles was presented in the high-resolution STEM (HRSTEM) images and fast Fourier transforms (FFTs) in our previous study [26] and is also shown in Figure 1. When they are sufficiently large, the Mn_3O_4 nano-islands appear to have a pyramidal shape grown preferentially on the {111} facets of the NiO core nanocrystals. For Mn_3O_4 nano-islands having considerably smaller size than the mean NiO core size, there does not appear to be a preferential overgrowth morphology. The lattice mismatch between the NiO core and Mn_3O_4 overgrowth phases, as determined from the fitted XRD data [26], is 2.2%. The NiO/Mn_3O_4 core/overgrowth interface from the HRSTEM imaging is generally shown to be flat and coherent (see Figure 1 and Ref. 26).

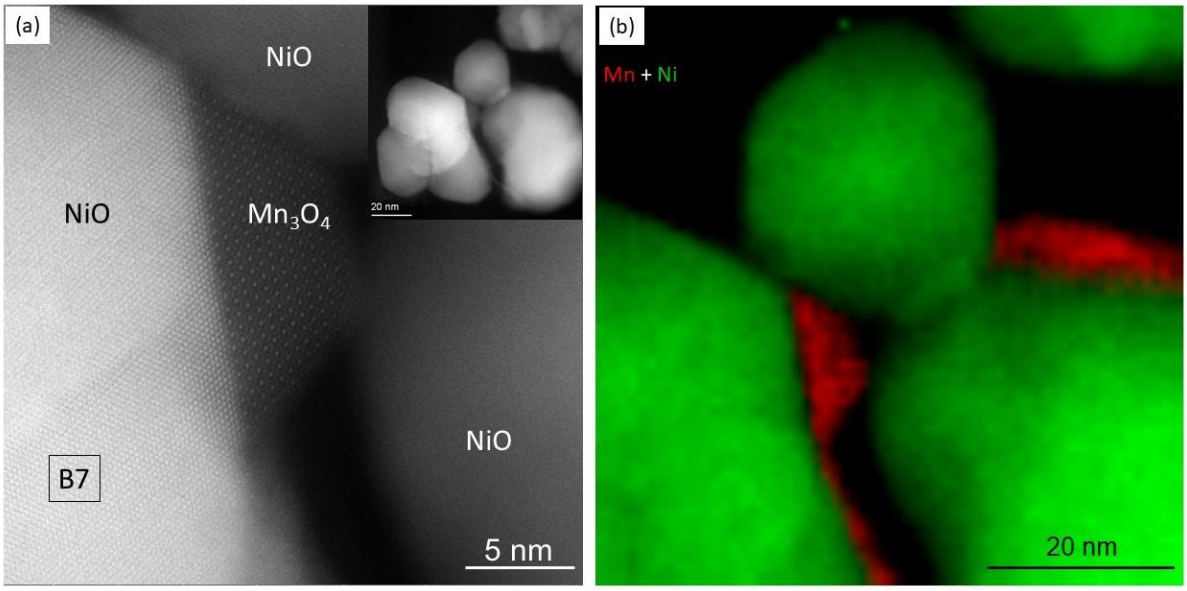

Fig. 1 (a) HRSTEM image of sample B7 showing Mn_3O_4 island overgrowth on a NiO nanoparticle; (b) STEM-EELS data of the central part of inset in (a) confirms the presence of Mn and Ni in the overgrowth and core regions of a cluster of HNCs of the same sample, respectively.

Ni 2p XPS spectra measured from NiO nanoparticles (A1) and from select HNC samples (B1, B3, B5, and B7) are shown in Figure 2. The 2p region is split into the $2p_{1/2}$ and $2p_{3/2}$ contributions due to spin-orbit coupling. Satellite peaks are the resultants of the shake-up effect that occurs due to the excitation of the photoelectron and deposition of the (kinetic) energy in the system by that particular photoelectron [37]. In NiO, the 2p photoemission electrons originating within the Ni^{2+} [(Ar) $3d^8$] oxidation state interact with electrons from the 3d shell, which results in a shake-up effect and generates the satellite peaks. The relative positions of the main $2p_{1/2}$ and $2p_{3/2}$ peaks and satellite peaks of all the samples shown in Figure 2 are listed in Table SI whereas the areas under the main and satellite peaks are shown in Table SII. As seen from Table SI, the Ni $2p_{1/2}$ and $2p_{3/2}$ peak binding energy (B.E.) positions are

consistent with a Ni^{2+} chemical environment in a rocksalt structure and well-ordered NiO or $Mn_xNi_{1-x}O$ nanomaterial for all samples. The small variations in the Ni 2p peak B.E. positions are attributed to experimental and analyses uncertainties. The primary satellite peaks are situated at approximately 7 eV higher binding energy from the main Ni 2p peak lines (see Figure 2). Furthermore, in agreement with Biju et. al, there is another set of satellite peaks for all samples located at 1.5 eV higher B.E. relative to the main Ni 2p lines [38]. In general, the satellite peaks are reduced in the Ni 2p-region of the XPS spectra in going from sample A1 (NiO nanoparticles) → B1 → B8. From their XPS measurements of bulk and nanoparticulate Fe_3O_4, Wilson et al., concluded that a reduction of similar satellite features in the Fe 2p XPS region for the nanoparticles resulted from their substantially smaller size and defects in the crystal structure [39]. According to the authors, owing to their substantial surface-to-volume ratio, under-coordination of cations and defects in nanoparticles results in a suppression of shake-up and related effects responsible for the satellite features. This is in good agreement with the general trend of particle size reduction in going from B1 to B8 as seen in Table I and from the trend of nanophase overlayer type (Mn_3O_4 and/or $Mn_xNi_{1-x}O$), where the more structurally mismatched Mn_3O_4 phase becomes more dominant with increasing pH used in the synthesis of the HNCs [26]. Because the surface-to-volume ratio is increased only by ~15%, it is plausible that the increase in defects, given the larger lattice mismatch between the NiO core and Mn_3O_4 overgrowth phases, is the dominant cause of the reduction of the satellite features in the Ni 2p spectra in going from sample B1 to B8.

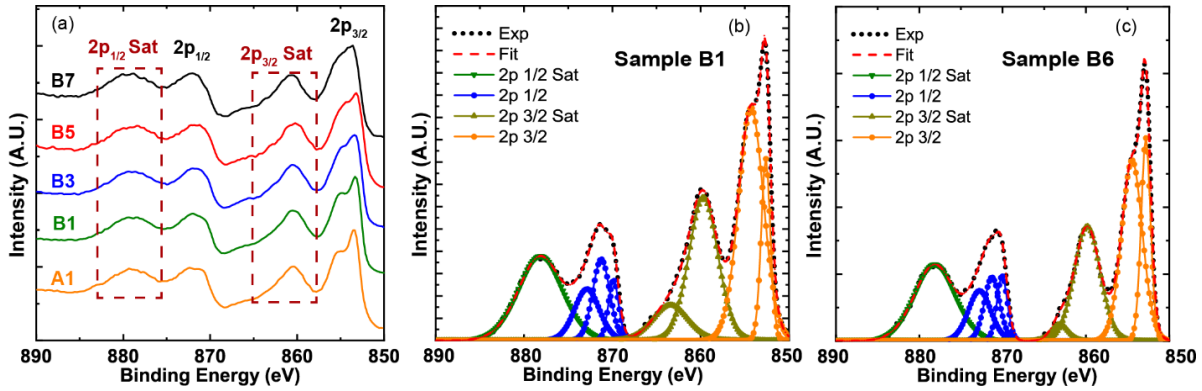

Fig. 2 (a) XPS spectra of the Ni 2p region measured from NiO nanoparticles (A1) and select HNC samples (B1, B3, B5, and B7). (b) Detailed peak fitting of the Ni 2p XPS spectra measured from sample B1, and (c) from sample B6.

The satellite peak occurring at 1.5 eV higher B.E. than the Ni $2p_{3/2}$ peak has been attributed to multiplet splitting [40–44]. Multiplet splitting occurs provided there are unfilled shells with lone pairs, such as in transition metals with partially filled p and d orbitals and rare-earth metals with partially filled f orbitals. It arises from the fact that an electron can have spin up/down states, the photoemissions from which are observed as separate peaks in XPS. In case of NiO, multiplet splitting is related to both local and non-local screening effects of the final state of the electronic structure manifested in the photoemission process. The lowest energy state for NiO is $2p^5\ 3d^9\ \underline{L}$ which occurs due to the nonlocal screening process ($2p^6\ 3d^8 + h\upsilon \rightarrow 2p^5\ 3d^9\ \underline{L} + e^-$) giving rise to the satellite peak at ~1.5 eV higher B.E. than the main 2p peaks [38,44]. Here $\underline{L}$ represents a valence band hole. Conversely, the main Ni 2p peaks occurring at ~853 eV and ~871 eV are generated due to a local screening process ($2p^6\ 3d^8 + h\upsilon \rightarrow \underline{2p}^5\ 3d^8 + e^-$), where $\underline{2p}^5$ represents a localized photon-induced hole. The multiplet fitting used to fit the Ni 2p region in the XPS spectra of select samples is shown in Figure 2(b) and (c). Additional Ni 2p fitted spectra are shown in Figures S1–S3.

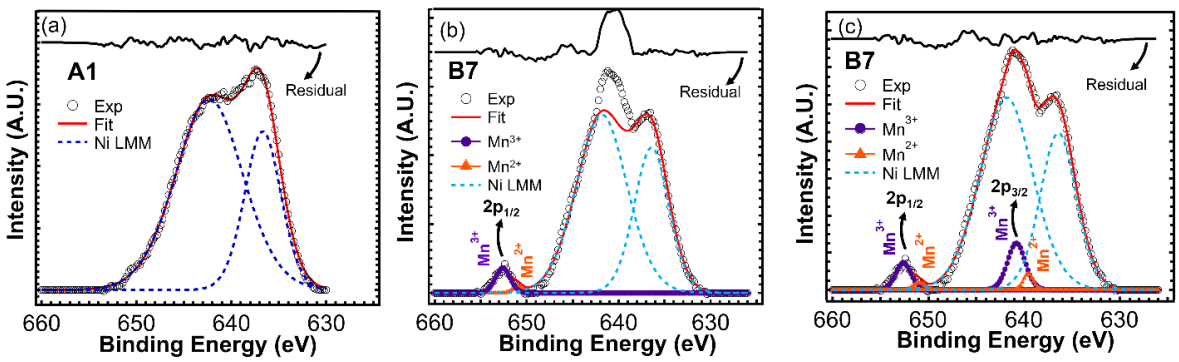

Fig. 3 (a) Fitted Ni Auger spectra for sample A1, (b) the Ni Auger contribution (solid line) and the Mn $2p_{3/2}$ signal shown above the Auger signal and in the resulting residual for sample B7. (c) Full peak fitting including the Mn $2p_{3/2}$ peaks along with the Ni LMM Auger peaks for sample B7.

XPS is an excellent spectroscopic tool for the determination of the elemental oxidation state, including that of Mn [45]. Our previous study showed that the conditions within the hydrothermal environment in the second synthesis step favor partial oxidation of Mn^{2+} to Mn^{3+} and deposition of Mn_3O_4 overgrowth on the NiO core nanoparticles with increasing pH [26]. The binding energy for the Mn $2p_{3/2}$ photoemission for manganese oxides (MnO, Mn_2O_3, Mn_3O_4) falls between 640.4 to 642.8 eV [46]. Furthermore, the LMM Auger electron peaks for the Ni 2p photoemission fall in the range between 636.3 eV to 643.1 eV of binding energy [41] [47]. As a result, the Ni Auger peaks merge and suppress the Mn $2p_{3/2}$ peaks making it difficult to identify the later peaks. We use an approach (described below) to accurately determine and subtract out the Ni Auger peak contributions in the XPS region overlapping with the Mn $2p_{3/2}$ peaks. Further use of a fixed peak area ratio of 1:2 between Mn $2p_{1/2}$ and Mn $2p_{3/2}$ peaks enables quantitative analysis of the Mn 2p XPS peaks. Note that Auger peaks are typically displayed versus their kinetic energy as Auger electrons are produced by auto-ionization [46]. Nevertheless, here we use binding energy in the figures to display both the XPS features and the Ni Auger peaks (after conversion from kinetic energy to binding energy for the latter). The Ni Auger peak data, analyzed using parameters provided in the NIST database, for several batches of NiO nanoparticles synthesized in our lab under identical conditions (all having approximately the same size) are shown in Table SIII [46]. From this, the average area ratio of Ni LMM peak 2 to peak 1 was calculated to be 1.80 whereas the average kinetic energy and average FWHM values of peak 2 and peak 1 are: 844.19 eV and 849.81 eV, 8.33 and 4.37, respectively. The conversion from kinetic energy to B.E. for the LMM Auger electrons yields 636.69 eV for peak 2 and 643.7 eV for peak 1. Although there is some variability of the LMM peak locations in energy, FWHM, and peak areas, most likely due to experimental and analyses uncertainties, the average values of these quantities are representative of our (Mn_3O_4 and/or $Mn_xNi_{1-x}O$)/NiO HNCs. The Ni LMM Auger peak positions, the FWHM value and the peak 2 to peak 1 area ratio were fixed at the above listed average values and used to fit the XPS features in the ~630 – 650 eV B.E. measured from samples B1 – B8. This approach is demonstrated in Figure 3. It is evident from Figure 3 that when the Ni LMM Auger region of the XPS spectrum measured from sample B7 is fitted using the fixed parameter values (i.e., average values listed above), the residual from the fit coincides precisely with the Mn $2p_{3/2}$ overall peak shape. Thus, by use of fixed parameter values for the Ni LMM Auger peaks, the Mn $2p_{3/2}$ peak contributions were isolated and fit for our HNC samples.

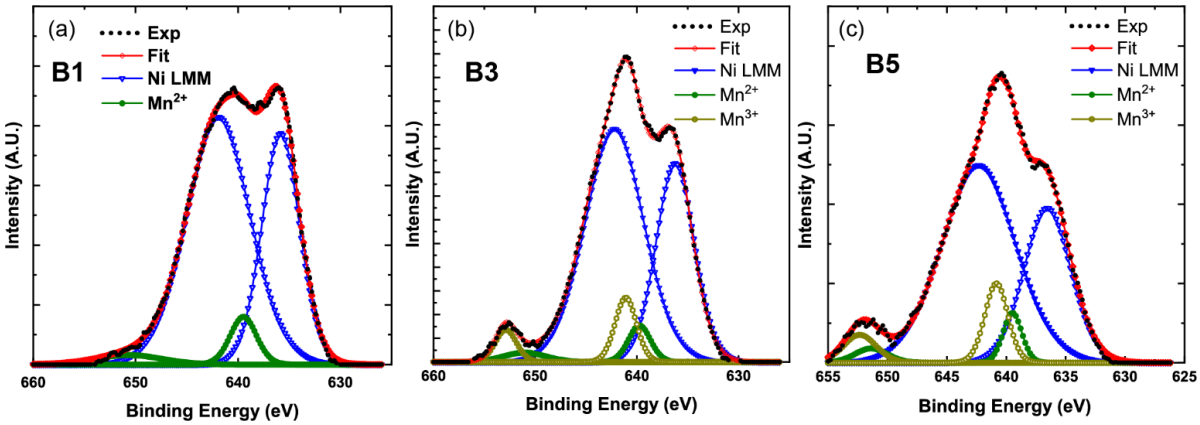

Fig. 4 Fitted Mn 2p XPS spectra shown for samples: (a) B1, (b) B3, and (c) B5.

As shown in previous studies, specific B.E. values and spacing (i.e., B.E. difference) between the Mn $2p_{1/2}$ and $2p_{3/2}$ constituent peaks is indicative of the valence state of manganese oxides [34,48–51]. Figure 4 shows the fitting of the Mn 2p region of the XPS spectra measured from samples B1, B3 and B7 whereas Table II shows that tabulation of the B.E. positions and B.E. differences between the Mn $2p_{1/2}$ and $2p_{3/2}$ constituent peaks for samples B1 – B8: Additional Ni LMM and Mn 2p fitted spectra measured from the remaining samples are shown in Figures S4-S5. As shown in Figure 4a, The Mn 2p region of the XPS spectrum measured from sample B1 has only one Mn $2p_{1/2}$ peak and one $2p_{3/2}$ peak with a B.E. difference of 11.3 eV between the two peaks, which is indicative of the Mn^{2+} oxidation state [34,48,50,51]. Conversely, analysis of the Mn 2p region of the XPS spectra measured from samples B3 and B7 show an additional pair of Mn $2p_{1/2}$ and a $2p_{3/2}$ constituent peaks with a B.E. difference between them of 11.8 eV, which is indicative of the Mn^{3+} oxidation state [34,48,50,51]. Thus, the XPS analysis results show that B1 only has Mn^{2+} present whereas sample B3 and B7 have both Mn^{2+} and Mn^{3+} cations present. Furthermore, peak fitting of the Mn 2p XPS region shows that the remaining B samples (B2, B4, B5, B6 and B8) also have both Mn^{2+} and Mn^{3+} cations present. In addition, the area of Mn 2p peaks associated with the Mn^{3+} oxidation state increase in proportion to the area the same peaks associated with the Mn^{2+} oxidation state, trending toward a 2:1 ratio, in the latter (B6 – B8) HNC samples. This is consistent with a predominance of the Mn_3O_4 overgrowth phase in the B6 – B8 samples. Overall, the results outlined above are consistent with our previous determination of the nature and prevalence of overgrowth phases present, from XRD, TEM and magnetometry measurements, in our HNC samples [26]. Yang et al. have speculated that the synergistic activity between $Mn3^{+}$ and $Ni2^{+}$, through oxygen bonding, leads to enhanced catalytic performance in Mn_3O_4-NiO heterostructured nanomaterials [34]. Provided this is indeed the case, our HNCs may provide suitable nanocomposite materials for heterogenous catalysis applications.

Table II: B.E. positions of the Mn $2p_{1/2}$ and $2p_{3/2}$ constituent peaks and their energy difference for samples B1 – B8

	Peak Position, B.E. (eV)			Peak Position, B.E. (eV)		
	Mn 2p1/2 peak 1	Mn 2p3/2 peak 1	Diff. eV	Mn 2p1/2 peak 2	Mn 2p3/2 peak 2	Diff. eV
B1	650.39	639.09	11.3	-	-	-
B2	651.63	640.23	11.4	653.13	641.23	11.9
B3	651.05	639.75	11.3	652.88	641.08	11.8
B4	652.78	641.28	11.5	654.18	642.48	11.7
B5	650.90	639.5	11.4	652.75	640.85	11.9
B6	649.97	638.37	11.6	652.23	640.13	12.1
B7	650.98	639.58	11.4	652.62	640.82	11.8
B8	651.47	639.97	11.5	652.82	641.02	11.8

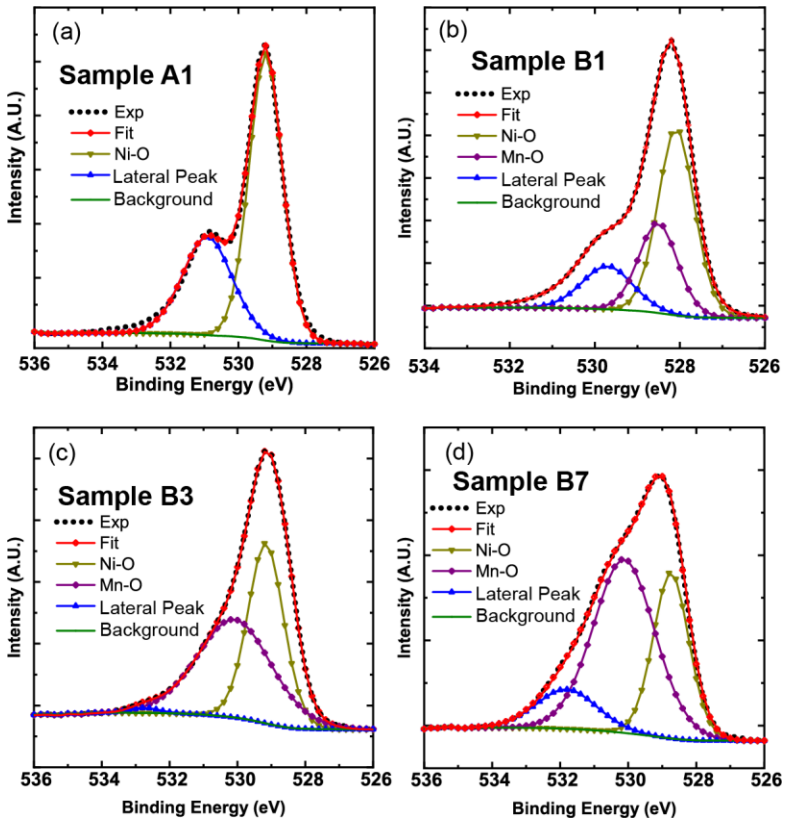

Fig. 5 Fitted O 1s region of the XPS spectra for samples (a) A1, (b) B1, (c) B3 and (d) B7.

Figure 5 shows the fitted O 1s XPS spectral region for the NiO nanoparticles (A1) and select HNC samples (B1, B3, and B7). Additional fitted O 1s XPS spectra for samples B2, B4, B5, B6, and B8 are presented in Figures S6–S8. The O 1s spectral region for sample A1 consists of two peaks, one at 529.2 eV and the second at 530.8 eV of binding energy. The lower binding energy peak is indicative of Ni-O bonding, being consistent with Ni^{2+} oxidation state and a chemical environment stemming from a NiO rocksalt structure. The higher binding energy (or lateral) peak has been attributed to Ni-OH bonding and oxygen residing in an oxygen deficient environment (e.g., NiO_x, $x<1$), including one having oxygen vacancies [52]. The Ni-OH bonding is reasonable due to hydroxylation that occurs in the aqueous medium during the synthesis procedures. The lateral peak generally shifts to slightly higher binding energy for B1 – B8 samples, indicating that in addition to Ni-OH bonding, Mn-OH bonding (~531.7 eV) is also present in the HNC samples [53,54]. Thus, the lateral peak is most likely dominated by Ni-OH/Mn-OH bonding contributions and less so by oxygens in an oxygen deficient environment and/or oxygen vacancy defects. In addition to the NiO and Ni-OH/Mn-OH peaks, the O1s XPS spectra of HNC samples also exhibit the Mn-O bonding peak at 529.0 eV binding energy. We observe that the Mn-O peak intensity increases with increasing pH of the synthesis medium of the HNC samples. This is in agreement with the general trend of the area of the Mn 2p peaks and with results from our previous study showing an increase with Mn content of the HNC samples with increasing pH of the synthesis medium. Overall, we find that XPS is a useful probe to investigate Ni and Mn oxidation states, chemical environment, and defects at the surface/interface of our heterostructured nanocrystals. Furthermore, the presence of oxygen vacancies, NiO_x, and other possible point defects, as well the Mn-multivalency in the Mn_3O_4 nanophase and core/overgrowth interface characteristics, indicate that our HNC samples may be suitable for heterogenous applications.

Conclusions

Analysis was made of XPS spectra measured from a series of NiO nanocrystals overgrown by Mn_3O_4 nano-islands and/or a $Mn_xNi_{1-x}O$ shell, depending upon pH conditions used to prepare the samples. To accomplish the Mn

2p XPS analysis, we applied a systematic and standardized NiO LMM Auger peak fitting to isolate and fit Mn $2p_{3/2}$ peaks. The oxidation states of Mn are identified from the binding energy positions, along with their difference, of the Mn $2p_{1/2}$ and Mn $2p_{3/2}$ peaks. Analysis of the Mn 2p XPS region shows that Mn^{2+} is highly predominant for the sample synthesized at pH 2.4, which is consistent with $Mn_xNi_{1-x}O$ shell overgrowth, whereas Mn^{3+} becomes more prevalent for samples synthesized at pH ~3 – 4 trending predominantly to a 2:1 ratio of Mn^{3+}:Mn^{2+} for samples prepared at pH ~4.5 – 7. This confirms a trend toward predominant $Mn_xNi_{1-x}O$ shell overgrowth at low pH (2.4) and toward predominant Mn_3O_4 overgrowth at higher pH values (~4.5 – 7) during hydrothermal synthesis of our HNCs [26]. The quantitative analysis of the XPS data shows a higher amount of Mn concentration for pH ~5 – 7, which is consistent with greater deposition of Mn-bearing overgrowth under these conditions. A progressive reduction of a satellite peak occurring at ~1.5 higher B.E. than the Ni 2p peaks, which is attributed to a combination of overall particle size reduction and defects in the near surface region, is observed for HNC samples synthesized under increasing pH conditions. High resolution STEM imaging shows the NiO/Mn_3O_4 core-overgrowth interface of select HNC samples to be flat and coherent. Analysis of the O 1s XPS spectra indicates that the lateral peak feature is most likely dominated by Ni-OH and Mn-OH contributions with a smaller contribution from oxygens in an oxygen deficient environment and/or oxygen vacancy defects. Further studies of the full range of our HNCs should be made to test their potential for heterogeneous catalysis. In this way, optimization for their catalytic efficiency may be made through pH-tunability.

Acknowledgements

AAS acknowledges partial support from the College of Natural and Applied Sciences at Missouri State University. The use of equipment in the Potsdam Imaging and Spectral Analysis Facility (PISA) is acknowledged. We especially thank the European Regional Development Fund and the State of Brandenburg for the Themis Z microscope (part of PISA). We appreciate the helpful comments from the reviewers which have significantly improved the manuscript.

Conflict of Interest: The authors declare that they have no conflict of interest.

References

[1] E. C. Scher, L. Manna, A. Paul Alivisatos, J. M. Kelly, A. Shluger, S. Kershaw, J. H. Harding, and A. M. Stoneham, *Shape Control and Applications of Nanocrystals*, Philos. Trans. R. Soc. A Math. Phys. Eng. Sci. **361**, 241 (2003).

[2] L. Carbone and P. D. Cozzoli, *Colloidal Heterostructured Nanocrystals: Synthesis and Growth Mechanisms*, Nano Today **5**, 449 (2010).

[3] P. D. Cozzoli and C. Nobile, *Colloidal Oxide-Based Heterostructured Nanocrystals* (Elsevier Inc., 2020).

[4] T. Zhu, S. G. Cloutier, I. Ivanov, K. L. Knappenberger, I. Robel, and F. Zhang, *Nanocrystals for Electronic and Optoelectronic Applications*, J. Nanomater. **2012**, 2012 (2012).

[5] Y. W. Jun, J. S. Choi, and J. Cheon, *Heterostructured Magnetic Nanoparticles: Their Versatility and High Performance Capabilities*, Chem. Commun. 1203 (2007).

[6] R. Scarfiello, C. Nobile, and P. D. Cozzoli, *Colloidal Magnetic Heterostructured Nanocrystals with Asymmetric Topologies: Seeded-Growth Synthetic Routes and Formation Mechanisms*, Front. Mater. **3**, 1 (2016).

[7] H. Zhong, T. Mirkovic, and G. D. Scholes, *Nanocrystal Synthesis*, Compr. Nanosci. Technol. **1**–**5**, 153 (2011).

[8] J. Liu, S. Z. Qiao, J. S. Chen, X. W. Lou, X. Xing, and G. Q. Lu, *Yolk/Shell Nanoparticles: New Platforms for Nanoreactors, Drug Delivery and Lithium-Ion Batteries*, Chem. Commun. **47**, 12578 (2011).

[9] P. Alivisatos, *The Use of Nanocrystals in Biological Detection*, Nat. Biotechnol. **22**, 47 (2004).

[10] D. S, *Application of Nanocrystals in Drug Delivery: An Overview*, Bull. Pharm. Res. **8**, 1 (2018).

[11] J. Gao, H. Gu, and B. Xu, *Multifunctional Magnetic Nanoparticles: Design, Synthesis, and Biomedical Applications*, Acc. Chem. Res. **42**, 1097 (2009).

[12] S. E. Ahn et al., *Write Current Reduction in Transition Metal Oxide Based Resistance-Change Memory*, Adv. Mater. **20**, 924 (2008).

[13] M. J. Lee et al., *Electrical Manipulation of Nanofilaments in Transition-Metal Oxides for Resistance-Based Memory*, Nano Lett. **9**, 1476 (2009).

[14] S. P. Pati, B. Bhushan, A. Basumallick, S. Kumar, and D. Das, *Exchange Bias and Suppression of Superparamagnetism of α-Fe Nanoparticles in NiO Matrix*, Mater. Sci. Eng. B Solid-State Mater. Adv. Technol. **176**, 1015 (2011).

[15] V. Skumryev, S. Stoyanov, Y. Zhang, G. Hadjipanayis, D. Givord, and J. Nogués, *Beating the Superparamagnetic Limit with Exchange Bias*, Nature **423**, 850 (2003).

[16] W. Yan et al., *Valence State-Dependent Ferromagnetism in Mn-Doped NiO Thin Films*, Adv. Mater. **24**, 353 (2012).

[17] J. Al Boukhari, L. Zeidan, A. Khalaf, and R. Awad, *Synthesis, Characterization, Optical and Magnetic Properties of Pure and Mn, Fe and Zn Doped NiO Nanoparticles*, Chem. Phys. **516**, 116 (2019).

[18] P. Mallick, C. Rath, A. Rath, A. Banerjee, and N. C. Mishra, *Antiferro to Superparamagnetic Transition on Mn Doping in NiO*, Solid State Commun. **150**, 1342 (2010).

[19] S. Layek and H. C. Verma, *Room Temperature Ferromagnetism in Mn-Doped NiO Nanoparticles*, J. Magn. Magn. Mater. **397**, 73 (2016).

[20] S. Dey, M. D. Hossain, R. A. Mayanovic, R. Wirth, and R. A. Gordon, *Novel Highly Ordered Core–Shell Nanoparticles*, J. Mater. Sci. **52**, 2066 (2017).

[21] M. D. Hossain, R. A. Mayanovic, S. Dey, R. Sakidja, and M. Benamara, *Room-Temperature Ferromagnetism in Ni(<scp>ii</Scp>)-Chromia Based Core–Shell Nanoparticles: Experiment and First Principles Calculations*, Phys. Chem. Chem. Phys. **20**, 10396 (2018).

[22] M. D. Hossain, S. Dey, R. A. Mayanovic, and M. Benamara, *Structural and Magnetic Properties of Well-Ordered Inverted Core-Shell α-Cr 2 O 3 / α-M x Cr 2-x O 3 (M=Co, Ni, Mn, Fe) Nanoparticles*, MRS Adv. **1**, 2387 (2016).

[23] M. D. Hossain, R. A. Mayanovic, R. Sakidja, and M. Benamara, *An Experimental and Theoretical Study of the Optical, Electronic, and Magnetic Properties of Novel Inverted α-Cr2O3atα-Mn0.35Cr1.65O2.94 Core Shell Nanoparticles*, J. Mater. Res. **32**, 269 (2017).

[24] M. D. Hossain, R. A. Mayanovic, R. Sakidja, M. Benamara, and R. Wirth, *Magnetic Properties of Core-Shell Nanoparticles Possessing a Novel Fe(II)-Chromia Phase: An Experimental and Theoretical Approach*, Nanoscale **10**, 2138 (2018).

[25] S. Hasan, R. A. Mayanovic, and M. Benamara, *Synthesis and Characterization of Novel Inverted NiO @ Ni x Mn 1-x O Core-Shell Nanoparticles*, MRS Adv. **2**, 3465 (2017).

[26] A. Al Shafe, M. D. Hossain, R. A. Mayanovic, V. Roddatis, and M. Benamara, *Tuning Exchange Coupling in NiO-Based Bimagnetic Heterostructured Nanocrystals*, ACS Appl. Mater. Interfaces **13**, 24013 (2021).

[27] T. Sugimoto, *Formation of Modoispersed Nano- and Micro-Particles Controlled in Size, Shape, and Internal Structure*, Chem. Eng. Technol. **26**, 313 (2003).

[28] S. Ghorbani Gorji, E. Ghorbani Gorji, and M. A. Mohammadifar, *Effect of PH on Turbidity, Size, Viscosity and the Shape of Sodium Caseinate Aggregates with Light Scattering and Rheometry*, J. Food Sci. Technol.

52, 1820 (2015).

[29] J. P. Jolivet, S. Cassaignon, C. Chanéac, D. Chiche, O. Durupthy, and D. Portehault, *Design of Metal Oxide Nanoparticles: Control of Size, Shape, Crystalline Structure and Functionalization by Aqueous Chemistry*, Comptes Rendus Chim. **13**, 40 (2010).

[30] X. Xie, Synthesis of Model Nanocatalysts for Industrial Applications, Technische Universität Berlin, 2014.

[31] P. Littlewood, Low Temperature Dry Reforming of Methane with Nickel Manganese Oxide Catalysts, Technische Universität Berlin, 2016.

[32] J. Liu, L. Jiang, T. Zhang, J. Jin, L. Yuan, and G. Sun, *Activating Mn3O4 by Morphology Tailoring for Oxygen Reduction Reaction*, Electrochim. Acta **205**, 38 (2016).

[33] L. Zhang, T. Tong, N. Wang, W. Ma, B. Sun, J. Chu, K. A. Lin, and Y. Du, *Facile Synthesis of Yolk-Shell Mn3O4 Microspheres as a High-Performance Peroxymonosulfate Activator for Bisphenol A Degradation*, Ind. Eng. Chem. Res. **58**, 21304 (2019).

[34] M. Yang, Q. Ling, R. Rao, H. Yang, Q. Zhang, H. Liu, and A. Zhang, *Mn3O4-NiO-Ni/CNTs Catalysts Prepared by Spontaneous Redox at High Temperature and Their Superior Catalytic Performance in Selective Oxidation of Benzyl Alcohol*, J. Mol. Catal. A Chem. **380**, 61 (2013).

[35] T. Imboon, J. Khumphon, K. Yotkuna, I. M. Tang, and S. Thongmee, *Enhancement of Photocatalytic by Mn3O4 Spinel Ferrite Decorated Graphene Oxide Nanocomposites*, SN Appl. Sci. **3**, (2021).

[36] M. El-Kemary, N. Nagy, and I. El-Mehasseb, *Nickel Oxide Nanoparticles: Synthesis and Spectral Studies of Interactions with Glucose*, Mater. Sci. Semicond. Process. **16**, 1747 (2013).

[37] P. Persson, S. Lunell, A. Szöke, B. Ziaja, and J. Hajdu, *Shake-up and Shake-off Excitations with Associated Electron Losses in X-Ray Studies of Proteins*, Protein Sci. **10**, 2480 (2009).

[38] V. Biju and M. Abdul Khadar, *Electronic Structure of Nanostructured Nickel Oxide Using Ni 2p XPS Analysis*, J. Nanoparticle Res. **4**, 247 (2002).

[39] D. Wilson and M. A. Langell, *XPS Analysis of Oleylamine/Oleic Acid Capped Fe 3 O 4 Nanoparticles as a Function of Temperature*, Appl. Surf. Sci. **303**, 6 (2014).

[40] M. C. Biesinger, B. P. Payne, A. P. Grosvenor, L. W. M. Lau, A. R. Gerson, and R. S. C. Smart, *Resolving Surface Chemical States in XPS Analysis of First Row Transition Metals, Oxides and Hydroxides: Cr, Mn, Fe, Co and Ni*, Appl. Surf. Sci. **257**, 2717 (2011).

[41] M. C. Biesinger, L. W. M. Lau, A. R. Gerson, and R. S. C. Smart, *The Role of the Auger Parameter in XPS Studies of Nickel Metal, Halides and Oxides*, Phys. Chem. Chem. Phys. **14**, 2434 (2012).

[42] A. P. Grosvenor, M. C. Biesinger, R. S. C. Smart, and N. S. McIntyre, *New Interpretations of XPS Spectra of Nickel Metal and Oxides*, Surf. Sci. **600**, 1771 (2006).

[43] M. C. Biesinger, B. P. Payne, L. W. M. Lau, A. Gerson, and R. S. C. Smart, *X-Ray Photoelectron Spectroscopic Chemical State Quantification of Mixed Nickel Metal, Oxide and Hydroxide Systems*, Surf. Interface Anal. **41**, 324 (2009).

[44] M. A. Peck and M. A. Langell, *Comparison of Nanoscaled and Bulk NiO Structural and Environmental Characteristics by XRD, XAFS, and XPS*, Chem. Mater. **24**, 4483 (2012).

[45] E. S. Ilton, J. E. Post, P. J. Heaney, F. T. Ling, and S. N. Kerisit, *XPS Determination of Mn Oxidation States in Mn (Hydr)Oxides*, Appl. Surf. Sci. **366**, 475 (2016).

[46] S. W. G. N. A. V. A. K.-V. C. J. Powell, *NIST X-Ray Photoelectron Spectroscopy Database*, 4.1

(Measurement Services Division of the National Institute of Standards and Technology (NIST) Technology Services, 2012).

[47] J. M. Sanz and G. T. Tyuliev, *An XPS Study of Thin NiO Films Deposited on MgO(100)*, Surf. Sci. **367**, 196 (1996).

[48] S. Xi, Y. Zhu, Y. Yang, S. Jiang, and Z. Tang, *Facile Synthesis of Free-Standing NiO/MnO2 Core-Shell Nanoflakes on Carbon Cloth for Flexible Supercapacitors*, Nanoscale Res. Lett. **12**, (2017).

[49] V. R. Galakhov, M. Demeter, S. Bartkowski, M. Neumann, N. A. Ovechkina, E. Z. Kurmaev, N. I. Lobachevskaya, Y. M. Mukovskii, J. Mitchell, and D. L. Ederer, *Mn (Formula Presented) Exchange Splitting in Mixed-Valence Manganites*, Phys. Rev. B - Condens. Matter Mater. Phys. **65**, 1 (2002).

[50] A. K. Shukla, P. Krüger, R. S. Dhaka, D. I. Sayago, K. Horn, and S. R. Barman, *Understanding the 2p Core-Level Spectra of Manganese: Photoelectron Spectroscopy Experiments and Anderson Impurity Model Calculations*, Phys. Rev. B - Condens. Matter Mater. Phys. **75**, 1 (2007).

[51] M. C. Biesinger, B. P. Payne, A. P. Grosvenor, L. W. M. Lau, A. R. Gerson, and R. S. C. Smart, *Resolving Surface Chemical States in XPS Analysis of First Row Transition Metals, Oxides and Hydroxides: Cr, Mn, Fe, Co and Ni*, Appl. Surf. Sci. **257**, 2717 (2011).

[52] J. C. Dupin, D. Gonbeau, P. Vinatier, and A. Levasseur, *Systematic XPS Studies of Metal Oxides, Hydroxides and Peroxides*, Phys. Chem. Chem. Phys. **2**, 1319 (2000).

[53] A. G. Marrani, F. Caprioli, A. Boccia, R. Zanoni, and F. Decker, *Electrochemically Deposited ZnO Films: An XPS Study on the Evolution of Their Surface Hydroxide and Defect Composition upon Thermal Annealing*, J. Solid State Electrochem. **18**, 505 (2014).

[54] H. W. Nesbitt and D. Banerjee, *Interpretation of XPS Mn(2p) Spectra of Mn Oxyhydroxides and Constraints on the Mechanism of MnO2 Precipitation*, Am. Mineral. **83**, 305 (1998).